Journal of Materials and Environmental Science
ISSN : 2028-2508
e-ISSN : 2737-890X
CODEN : JMESCN
Copyright © 2026,

J. Mater. Environ. Sci., 2026, Volume 17, Issue 10, Page 1483-1497

http://www.jmaterenvironsci.com

Valorization of Agro-Industrial Cocoa Pod Residues into Optimized Activated Carbon for Simultaneous Aqueous Heavy Metal and Dye Remediation

Mouafo Mouafo F. J. [12*], Ankoro N. O. [1], Appiah Kouassi E.K [2], Ndi J. N. [1*], Ngomo H. M. [1]

[1]*Applied Physical and Analytical Chemistry Laboratory, Department of Inorganic Chemistry, Faculty of Science, University of Yaoundé I, P.O. Box 812, Yaoundé, Cameroon*

[2] *Laboratory of Industrial Process Synthesis, Environmental and New Energy (LAPISIEN) at the Institut National Polytechnique Félix Houphouët-Boigny, Yamoussoukro, Côte d'Ivoire*

**Corresponding author, Email address: mouafofranckjoel@yahoo.fr*

Received *30 July 2026,*
Revised *19 Oct 2026,*
Accepted *23 Oct 2026*

Keywords:
✓ *Optimization;*
✓ *Cocoa pod;*
✓ *Activated carbon;*
✓ *Indigo carmine;*
✓ *Copper(II) ions.*

Citation: *Mouafo Mouafo F. J., Ankoro N. O., Appiah Kouassi E.K., Ndi J. N., Ngomo H. M. (2026) Valorization of Agro-Industrial Cocoa Pod Residues into Optimized Activated Carbon for Simultaneous Aqueous Heavy Metal and Dye Remediation, J. Mater. Environ. Sci., 17(10), 1483-1497.*

Abstract: The optimization of the preparation of activated carbon derived from cocoa pods was conducted using a Box-Behnken experimental design. The optimal preparation conditions determined were a residence time of 1 hour, an impregnation ratio (H_3PO_4/precursor) of 1.3, and a carbonization temperature of 333 °C. The synthesized activated carbon (ACP) was characterized using Scanning Electron Microscopy (SEM), Thermogravimetric Analysis (TGA-DSC), and Fourier Transform Infrared Spectroscopy (FTIR). Batch adsorption results demonstrated that maximum adsorption capacities were achieved at pH 2.0 for Indigo Carmine (IC) dye (80.42 mg/g) and pH 4.5 for copper(II) ions (167.50 mg/g). The adsorption capacity increased with rising initial adsorbate concentration and decreased with increasing adsorbent mass. Nonlinear regression analyses of equilibrium isotherms indicated that none of the classical two-parameter models (Langmuir, Freundlich, Temkin, Dubinin-Radushkevich) fully described the equilibrium mechanism across the entire concentration range due to moderate determination coefficients (R^2 = 0.504–0.768). Conversely, kinetic modeling revealed that the Elovich model best describes the adsorption process for both adsorbates, yielding determination coefficients close to unity (R^2 = 0.979 for IC and R2 = 0.991 for Cu(II)). FTIR spectra recorded before and after adsorption confirmed the active involvement of oxygenated and phosphorus-containing surface functional groups, substantiating chemisorption on an energetically heterogeneous surface as the predominant mechanism.

1. Introduction

In recent decades, rapid industrialization and urbanization driven by population growth have resulted in severe water contamination through the discharge of massive volumes of solid and liquid wastes (Zulfiqar *et al.*, 2019). Driven by increasing industrial demand, sectors such as textiles, pharmaceuticals, metallurgy, petrochemicals, cosmetics, plastics, and food processing utilize a wide array of synthetic dyes and heavy metals (Harrache *et al.*, 2019), frequently releasing untreated effluents into aquatic ecosystems. Most synthetic organic dyes and transition metal ions are chemically and thermally stable, non-biodegradable, and highly toxic (León *et al.*, 2018; Ahmadi and Ganjidoust, 2021; Berrahou *et al.*, 2026. Polluted wastewater inflicts long-term ecological damage and threatens human health with carcinogenic, mutagenic, and nephrotoxic effects. Consequently, the effective remediation of dyes and heavy metals from aqueous effluents remains a critical environmental challenge (Li *et al.*, 2016).

To mitigate the presence of hazardous pollutants such as copper(II) ions and indigo carmine (IC) dye prior to environmental discharge, numerous physicochemical treatment technologies have been developed, including chemical precipitation, ion exchange, membrane filtration, electrochemical processes, coagulation-flocculation, reverse osmosis, and adsorption (Ngaha *et al.*, 2019; Ahmadi and Ganjidoust, 2021). Among these methods, liquid-phase adsorption is widely recognized as technically superior, cost-effective, simple to operate, and capable of removing a broad spectrum of organic and inorganic contaminants without generating toxic sludge (Ankoro *et al.*, 2020; Mashile *et al.*, 2021; Rashid *et al.*, 2021).

Although commercial activated carbon is the benchmark adsorbent in wastewater treatment, its prohibitive production cost limits its large-scale deployment in developing economies (Athéba *et al.*, 2015). To address this constraint, extensive research has focused on valorizing abundant, low-cost lignocellulosic agricultural residues as activated carbon precursors. Utilizing agro-industrial waste serves a dual purpose: manufacturing high-performance adsorbents economically while adding value to local agricultural by-products (Ousmaila *et al.*, 2016). Various biomass precursors have been investigated, including banana peels, orange peels, cassava peels, peanut shells, bamboo shoots, coconut shells, egusi seed shells, and cocoa pods (Wong *et al.*, 2018; Hashem *et al.*, 2020; Ahmadi and Ganjidoust, 2021; Jiang *et al.*, 2021).

Cocoa pods (*Theobroma cacao* L.) constitute a particularly attractive precursor due to their massive global availability, with annual worldwide cocoa bean production reaching approximately 5,252,377 tonnes (FAOSTAT, 2020) and 335,850 tonnes in Cameroon alone (DESA, 2020). Because cocoa pod husks represent roughly 70–75% of the fresh fruit weight and are typically discarded in plantations, converting them into chemically activated carbon offers a sustainable waste-management and water-treatment pathway. The objective of this study is to optimize the H_3PO_4-assisted chemical activation of cocoa pods via Response Surface Methodology (Box-Behnken design), characterize the physicochemical properties of the resulting adsorbent (TGA-DSC, FTIR, SEM, and pHPZC), and evaluate its equilibrium and kinetic adsorption performance toward Indigo Carmine dye and Cu(II) ions.

2. Methodology

2.1 Sourcing and preparation of activated carbon

Raw cocoa pods rich in cellulose, hemicellulose, and lignin were collected from plantations in the Elat district (Nkol-Afamba sub-division, Mfoundi division, Central Region of Cameroon, east of Yaoundé). These cocoa pods represent a major unvalorized agricultural residue (**Figure 1**). The harvested pods were thoroughly washed under running tap water to remove surface impurities, rinsed with distilled water, chopped into small fragments, and sun-dried for three weeks. The dried biomass was crushed and sieved to isolate particles with sizes ranging between 1.25 and 2.50 mm.



Figure 1. Fresh and dried cocoa pod husks used as precursor material.

Chemical activation was carried out using orthophosphoric acid (H_3PO_4, 85%) at a mass impregnation ratio (r) defined by **Eqn. 1**:

$$r = m_cocoa_pod / m_H_3PO_4 \qquad \textbf{Eqn. 1}$$

Following impregnation, the precursor mixture was oven-dried at 110 °C for 24 h. Carbonization was conducted in a muffle furnace at programmed temperatures (300–500 °C) and residence times (1–2 h) at a constant heating rate of 10 °C/min, followed by gradual cooling to ambient temperature. The resulting carbonized materials were repeatedly washed with distilled water until a neutral filtrate pH (~6.5–7.0) was attained, then dried at 110 °C for 24

h. Finally, the activated carbon (ACP) was ground in a porcelain mortar, sieved to a particle size < 75 µm, and stored in airtight glass bottles inside a desiccator.

2.2 Box-Behnken experimental design optimization

A three-factor, three-level Box-Behnken Design (BBD) was established using Minitab 16 software (Minitab Inc., USA) to optimize the preparation parameters: carbonization temperature (A), residence time (B), and impregnation ratio (C). The experimental domain and coded levels are presented in **Table 1**, while the complete 15-run randomized experimental matrix (including three center-point replicates to evaluate pure error and reproducibility) is detailed in **Table 2**. Three response variables were monitored: Iodine Number (Y1, mg/g), Methylene Blue Number (Y2, mg/g), and Carbonization Yield (Y3, %). Experimental data were fitted to a second-order polynomial model and validated via Analysis of Variance (ANOVA) at the 95% confidence level.

Table 1. Experimental factors, symbols, units, and coded levels for the Box-Behnken design.

Natural variables	Coded variables	Units	Level -1	Level 0	Level +1
Carbonization temperature	A	°C	300	400	500
Residence time	B	h (min)	1.0 (60)	1.5 (90)	2.0 (120)
Impregnation ratio	C	g/g	1.0	1.5	2.0

Table 2. Box-Behnken experimental matrix with coded and actual process variables.

Run N°	Block	Coded A	Coded B	Coded C	Temperature (°C)	Time (h)	Ratio (g/g)
1	1	-1	-1	0	300	1.0	1.5
2	1	+1	-1	0	500	1.0	1.5
3	1	-1	+1	0	300	2.0	1.5
4	1	+1	+1	0	500	2.0	1.5
5	1	-1	0	-1	300	1.5	1.0
6	1	+1	0	-1	500	1.5	1.0
7	1	-1	0	+1	300	1.5	2.0
8	1	+1	0	+1	500	1.5	2.0
9	1	0	-1	-1	400	1.0	1.0
10	1	0	+1	-1	400	2.0	1.0
11	1	0	-1	+1	400	1.0	2.0
12	1	0	+1	+1	400	2.0	2.0
13	1	0	0	0	400	1.5	1.5
14	1	0	0	0	400	1.5	1.5
15	1	0	0	0	400	1.5	1.5

2.3 Physicochemical characterization and batch adsorption experiments

Surface functional groups of raw cocoa pods and ACP (before and after adsorption) were analyzed via Fourier Transform Infrared Spectroscopy (FTIR) in the mid-infrared range (400–4000 cm^{-1}) at the Laboratory of Analytical Chemistry, University of Yaoundé I. Thermogravimetric and Differential Scanning Calorimetry (TGA/DSC) analyses were carried out at the Laboratory of Materials Chemistry, University of Yaoundé I, to evaluate thermal mass-loss profiles. The point of zero charge (pHPZC) was determined by contacting 0.1 g of ACP with 40 mL of 0.1 M NaCl solutions adjusted between pH 2.0 and 10.0 using 0.1 N HCl or NaOH. Surface morphology was examined via Scanning Electron Microscopy (SEM) at an accelerating voltage of 5.00 kV and magnification of 10,000×.

Stock solutions of Indigo Carmine (IC, 1000 mg/L) and Copper(II) ions (4000 mg/L from $CuSO_4 \cdot 5H_2O$) were prepared in distilled water and diluted to working concentrations. Batch adsorption experiments were conducted at room temperature by agitating 0.02 g of ACP with 20 mL of adsorbate solution at constant stirring speed. After filtration through Whatman filter paper, residual concentrations were quantified spectrophotometrically at λmax = 610 nm (for IC) and λmax = 804 nm (for Cu(II)). The equilibrium adsorption capacity (Qe, mg/g) was computed using **Eqn. 2**:

$$Qe = ((C_0 - C_e) \times V) / m \quad \textbf{Eqn. 2}$$

where C_0 and C_e are the initial and equilibrium liquid-phase concentrations (mg/L), V is the solution volume (L), and m is the dry mass of ACP (g).

3. Results and Discussion

3.1 Characterization of the adsorbent material

The TGA-DSC thermogram of raw cocoa pod biomass (**Figure 2**) revealed four main thermal decomposition stages: (i) an endothermic dehydration peak at 77 °C corresponding to a 7.93% moisture loss (Lékéné *et al.*, 2018); (ii) an exothermic transition between 273 and 295 °C associated with hemicellulose decomposition (cumulative mass loss of 53.46%; Zhu *et al.*, 2016); (iii) an exothermic peak at 404 °C corresponding to cellulose pyrolysis (16.87% mass loss; Zhu *et al.*, 2016); and (iv) lignin degradation around 442 °C (5.72% mass loss; Lékéné *et al.*, 2018). These thermal profiles confirm that carbonization between 300 and 500 °C effectively devolatilizes non-carbon heteroatoms while preserving a stable carbon skeleton.

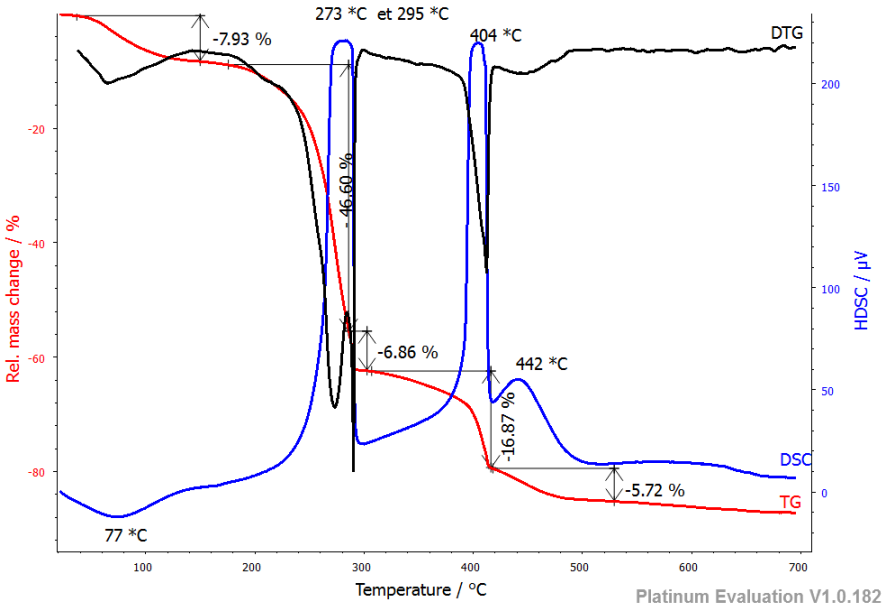


Figure 2. TGA-DSC and DTG thermograms of raw cocoa pod biomass.

The FTIR spectrum of raw cocoa pods (**Figure 3**) displayed characteristic lignocellulosic absorption bands at 3272 cm^{-1} (-OH stretching of alcohols, phenols, and carboxylic acids), 2929 cm^{-1} (aliphatic -C-H stretching), 1728 cm^{-1} (-C=O stretching of aldehydes/esters), 1369–1235 cm^{-1} (-C-O-C- ether vibrations), and 1029 cm^{-1} (aliphatic -C-O stretching) (Ankoro *et al.*, 2020). After H_3PO_4 activation, the ACP spectrum showed marked attenuation of the broad -OH band due to dehydration and cross-linking, alongside distinct bands at 2920 cm^{-1} (-C-H), 1705–1630 cm^{-1} (conjugated -C=O and aromatic -C=C- stretching), 1161 cm^{-1} (-C-O), and 1070 cm^{-1}, which is diagnostic of ionized linkage $-P^{+}-O^{-}$ in acid phosphate esters or -P=O stretching vibrations induced by phosphoric acid activation (Puziy *et al.*, 2005). SEM micrographs of ACP at 10,000× magnification (**Figure 4**) revealed an irregular, rough, and deeply pitted external surface containing abundant heterogeneous cavities and macroporous channels, confirming that H_3PO_4 acts as an effective dehydrating and pore-forming template during pyrolysis.

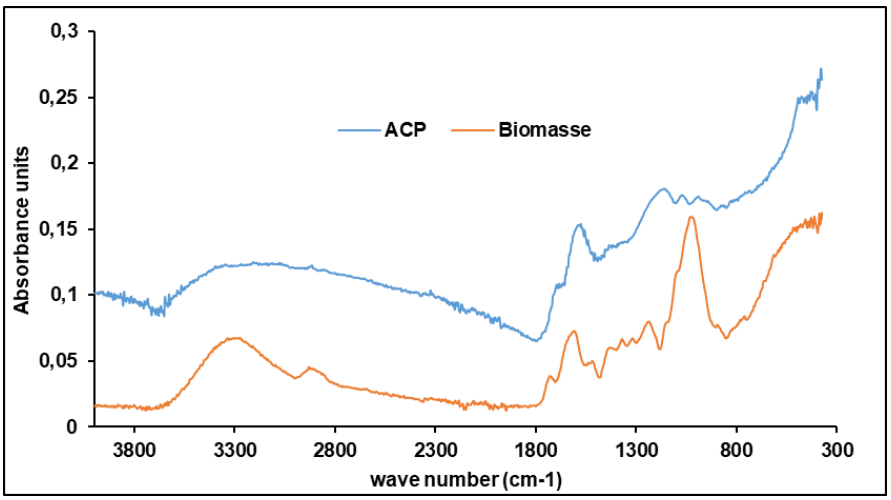


Figure 3. FTIR spectra of raw cocoa pod biomass and H_3PO_4-activated carbon (ACP).

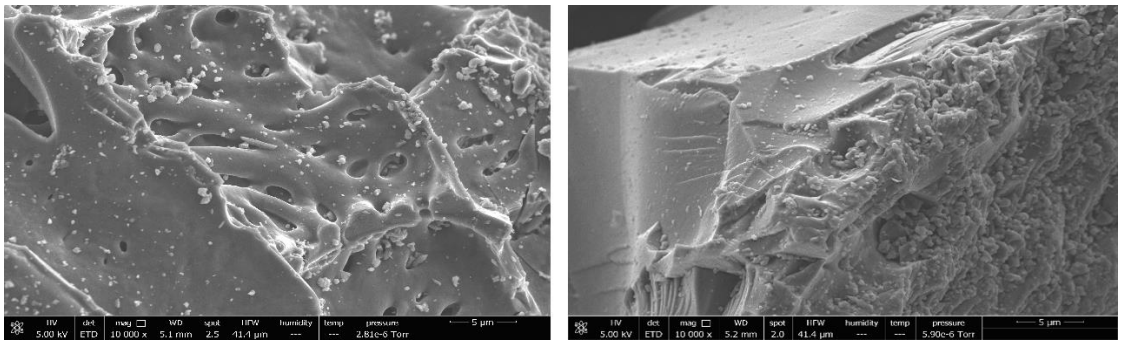


Figure 4. SEM micrographs of optimized cocoa pod activated carbon (ACP) at 10,000× magnification.

3.2 Box-Behnken optimization and statistical modeling

Experimental and model-predicted values for Iodine Number (Y1), Methylene Blue Number (Y2), and Carbonization Yield (Y3) across all 15 runs are compiled in **Table 3**. Yield varied from 40.00% to 60.00%, IN ranged from 480.66 to 785.46 mg/g, and MBN ranged from 46.98 to 89.85 mg/g.

Table 3. Experimental and predicted responses for the preparation of H3PO4-activated carbon (ACP).

Run	Temp (°C)	Time (h)	Ratio	IN Exp	IN Pred	MBN Exp	MBN Pred	Yield Exp (%)	Yield Pred (%)
1	300	1.0	1.5	543.53	539.24	66.41	64.75	53.30	54.10
2	500	1.0	1.5	694.02	685.45	89.85	90.99	42.66	45.87
3	300	2.0	1.5	579.72	588.29	80.57	79.43	60.00	56.79
4	500	2.0	1.5	781.65	785.94	89.85	91.51	48.00	47.20
5	300	1.5	1.0	577.82	580.44	88.65	87.11	51.00	50.58
6	500	1.5	1.0	735.93	742.84	89.85	85.51	46.00	43.17
7	300	1.5	2.0	480.66	473.76	46.98	51.32	48.00	50.83
8	500	1.5	2.0	657.83	655.21	89.70	91.24	40.00	40.42
9	400	1.0	1.0	638.78	640.44	89.83	93.04	45.00	44.62
10	400	2.0	1.0	785.46	774.27	89.83	92.51	44.00	47.63
11	400	1.0	2.0	591.15	602.34	72.57	69.89	48.00	44.37
12	400	2.0	2.0	619.73	618.06	88.82	85.62	45.00	45.38
13	400	1.5	1.5	554.96	554.98	89.82	89.78	42.53	42.62
14	400	1.5	1.5	554.96	554.96	89.76	89.78	42.66	42.62
15	400	1.5	1.5	554.96	554.96	89.76	89.78	42.66	42.62

The second-order empirical regression equations established in terms of actual factors—Temperature (A), Time (B), and Ratio (C)—are given in **Eqn. 3**, **Eqn. 4**, and **Eqn. 5**:

$$Y_Yield = 140.653 - 0.377A - 38.010B + 18.890C + 15.247B^2 - 3.713C^2 - 0.007AB - 0.015AC - 2.000BC \quad \textbf{Eqn. 3}$$

$$Y_IN = 1517.250 - 1.630A - 693.910B - 360.990C + 280.990B^2 + 134.300C^2 + 0.260AB + 0.100AC - 118.110BC \quad \textbf{Eqn. 4}$$

$$Y_MBN = 23.955 + 0.4737A + 21.4025B - 78.0825C - 0.0007A^2 - 3.285B^2 - 14.785C^2 - 0.0708AB + 0.2076AC + 16.250BC \quad \textbf{Eqn. 5}$$

The ANOVA statistical parameters and determination coefficients summarized in **Table 4** and **Table 5** demonstrate highly significant quadratic models for Iodine Number (F = 117.07, p = 0.000, R^2 = 99.53%, R^2adj = 98.68%) and Methylene Blue Number (F = 13.51, p = 0.005, R^2 = 96.05%, R^2adj = 88.94%). Normal probability plots of standardized residuals (**Figure 5**) closely follow a straight line, validating residual normality.

Table 4. Summary of ANOVA results for Yield (%R), Iodine Number (IN), and Methylene Blue Number (MBN).

Response	Source	DF	Seq SS	Adj SS	Adj MS	F-value	p-value
Yield (%R)	Regression	9	303.711	303.711	33.746	2.60	0.153
	Residual Error	5	64.913	64.913	12.983	—	—
	Total	14	368.623	—	—	—	—
Iodine Number	Regression	9	115677.0	115677.0	12853.0	117.07	0.000**
	Linear	3	89176.0	8466.0	2822.1	25.71	0.002**
	Square	3	22261.0	22261.0	7420.5	67.59	0.000**
	Interaction	3	4240.0	4240.0	1413.2	12.87	0.009**
	Residual Error	5	549.0	549.0	109.8	—	—
	Total	14	116226.0	—	—	—	—
MB Number	Regression	9	2080.960	2080.960	231.218	13.51	0.005**
	Linear	3	1301.160	255.290	85.097	4.97	0.058*
	Square	3	232.680	232.680	77.560	4.53	0.069*
	Interaction	3	547.120	547.120	182.373	10.66	0.013**
	Residual Error	5	85.550	85.550	17.111	—	—
	Total	14	2166.510	—	—	—	—

Table 5. Regression determination coefficients (R^2, R^2pred, and R^2adj) for the three response models.

Response	R^2	R^2 (pred)	R^2 (adj)
Yield (%R)	82.39%	0.00%	50.69%
Iodine Number (mg/g)	99.53%	92.44%	98.68%
Methylene Blue Number (mg/g)	96.05%	36.82%	88.94%

3D response surface and 2D contour plots (**Figures 6–9**) show that IN increases with carbonization temperature and residence time due to volatile release and micropore creation, whereas excessive H_3PO_4 ratios decrease IN via phosphate pore blockage and micropore widening into mesopores (Lékéné *et al.*, 2018; Kouotou *et al.*, 2013). Conversely, MBN increases proportionally with temperature and impregnation ratio, confirming mesopore expansion favorable for bulky dye molecules. Yield decreases at elevated temperatures due to intensified devolatilization (CO_2, CO, H_2O, CH_4) and thermal reduction of phospho-carbonaceous complexes (Ahmad and Alrozi, 2010). Desirability optimization established the optimal synthesis parameters at impregnation ratio = 1.3, carbonization temperature = 333 °C, and residence time = 1 hour.

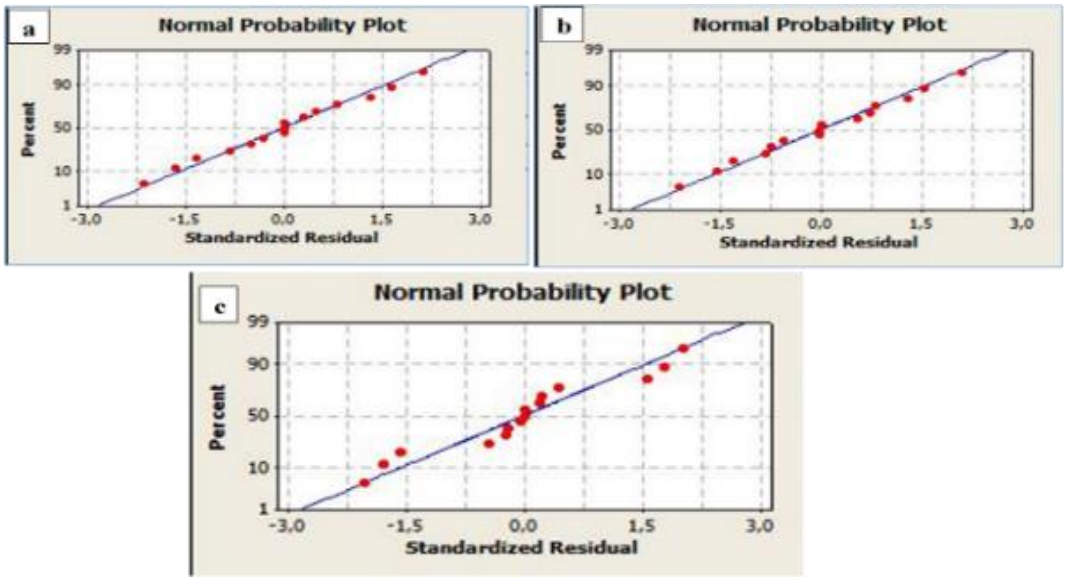


Figure 5. Normal probability plots of standardized residuals for (a) Yield, (b) Iodine Number, and (c) Methylene Blue Number.

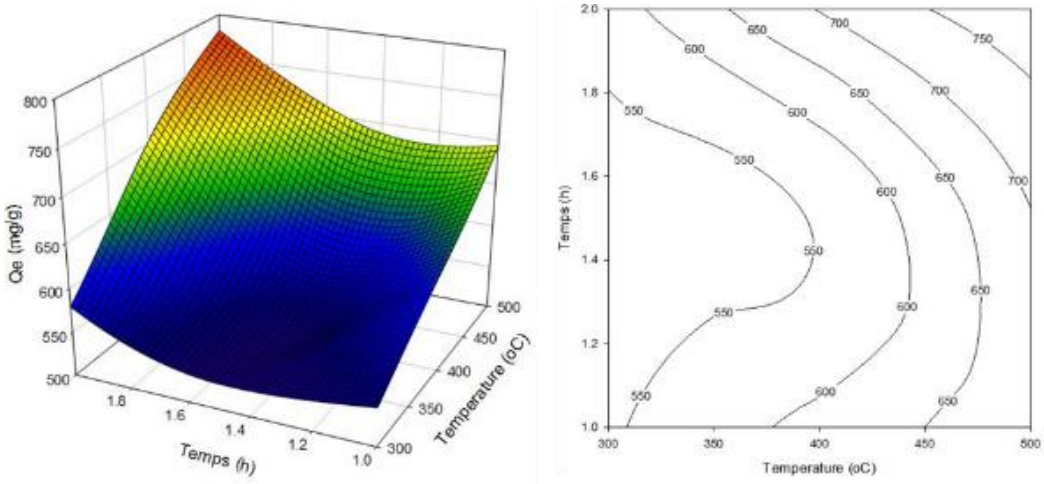


Figure 6. 3D response surface and 2D contour plot of Iodine Number (IN): Time–Temperature interaction.

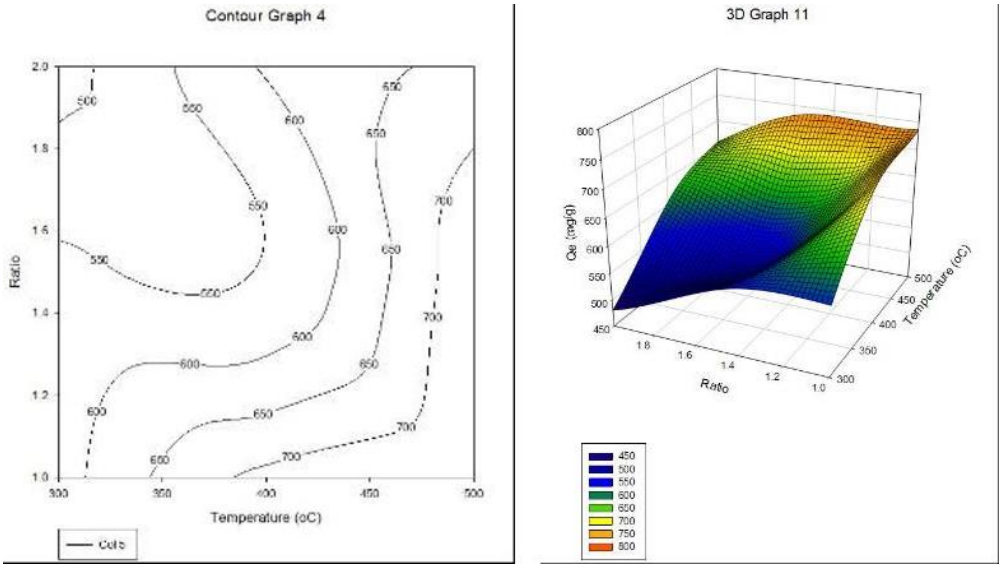


Figure 7. 2D contour and 3D response surface plots of Iodine Number (IN): Ratio–Temperature interaction.

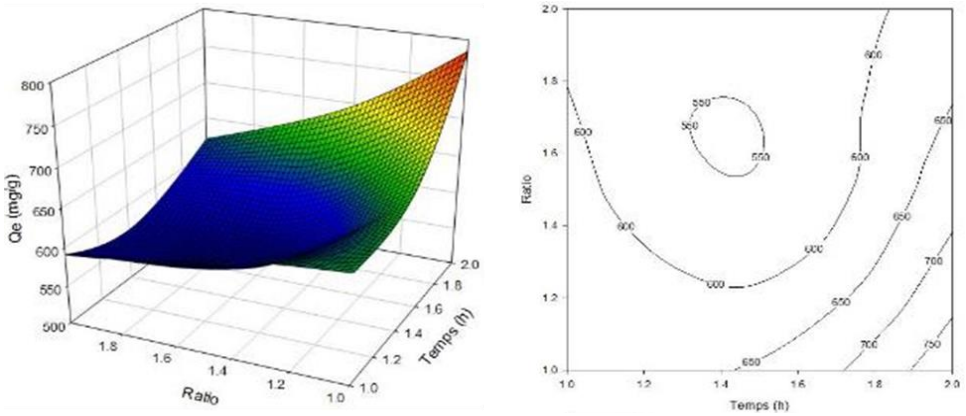


Figure 8. 3D response surface and 2D contour plot of Methylene Blue Number (MBN): Time–Ratio interaction.

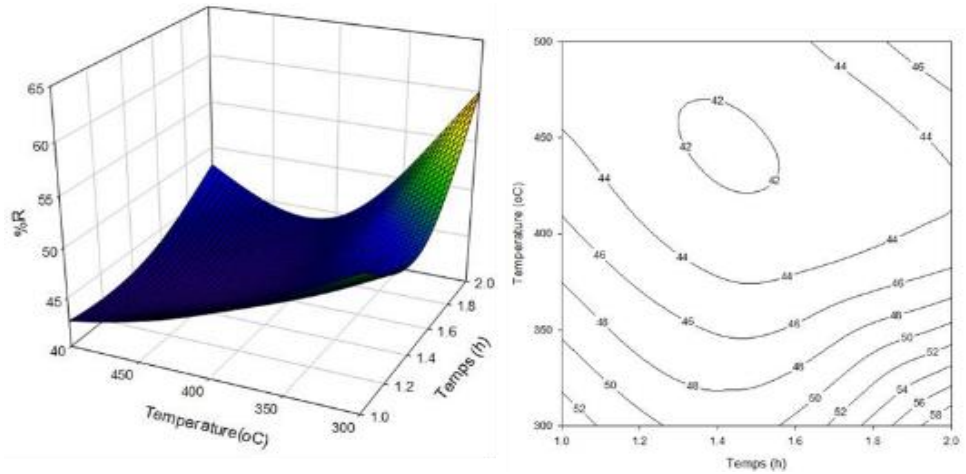


Figure 9. 3D response surface and 2D contour plot of Carbonization Yield (%R): Time–Temperature interaction.

3.3 Point of zero charge (pHPZC) and batch adsorption studies

The point of zero charge of ACP was determined to be pHPZC = 3.55 (**Figure 10**), confirming the predominance of acidic surface functionalities (carboxylic, phenolic, and phosphate groups). Consequently, the ACP surface carries a net positive charge at pH < 3.55 (favoring electrostatic attraction of anionic pollutants) and a net negative charge at pH > 3.55 (favoring cationic metal uptake) (Maazou *et al.*, 2017; Akartasse *et al.*, 2022).

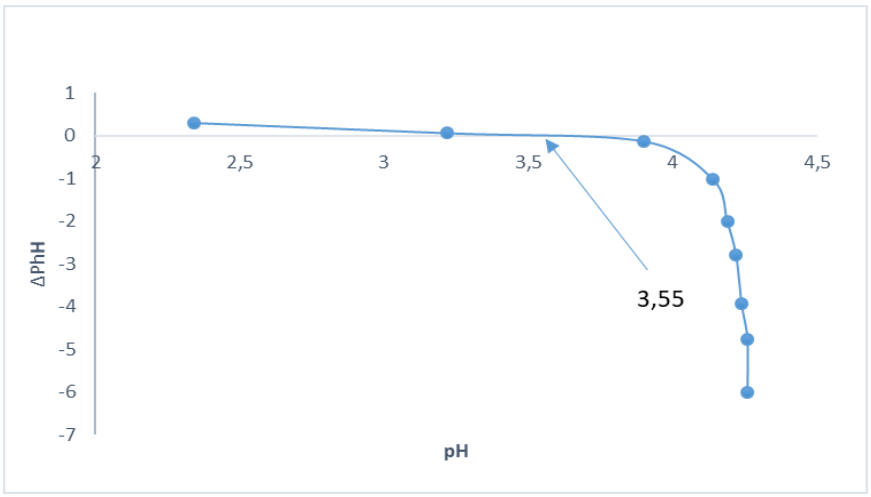


Figure 10. Determination of the point of zero charge (pHPZC = 3.55) of optimized ACP.

For Indigo Carmine (**Figure 11**), maximum uptake (74.40 mg/g at C_0 = 80 mg/L) occurred at pH 2.0, where strong protonation of surface groups promotes electrostatic attraction with anionic sulfonate (-SO_3-) groups (Ndifor-Angwafor *et al.*, 2017; Ngaha *et al.*, 2019). For Cu(II) ions (**Figure 12**), uptake increased sharply from pH 3.0 to reach 87.50 mg/g (at C_0 = 1000 mg/L) at pH 4.5, overcoming H^+ competition while avoiding $Cu(OH)_2$ precipitation above pH 5.0 (Abéga *et al.*, 2015). Increasing initial IC (50–100 mg/L, **Figure 13**) and Cu(II) concentrations (600–

1600 mg/L, **Figure 14**) enhanced adsorption capacities up to 80.42 mg/g and 167.50 mg/g, respectively, driven by a stronger concentration gradient overcoming liquid-solid mass transfer resistance (Abo El Naga *et al.*, 2019; Arivoli *et al.*, 2009). As shown in **Table 6**, optimized cocoa pod ACP exhibits superior Cu(II) adsorption capacity compared to numerous reported agricultural waste adsorbents.

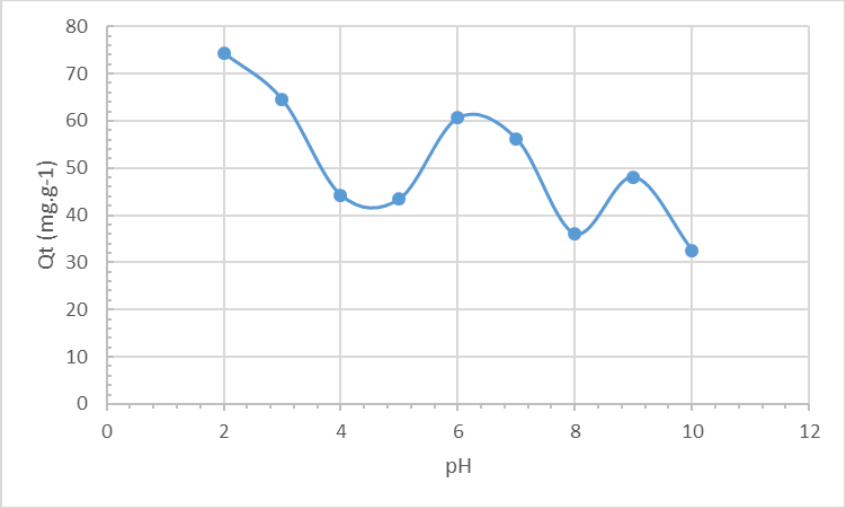


Figure 11. Influence of initial solution pH on Indigo Carmine (IC) adsorption onto ACP.

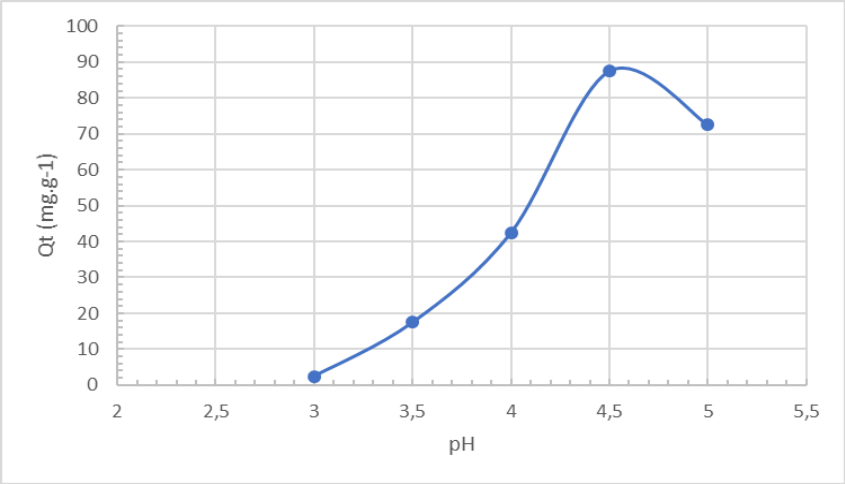


Figure 12. Influence of initial solution pH on Copper(II) ion adsorption onto ACP.

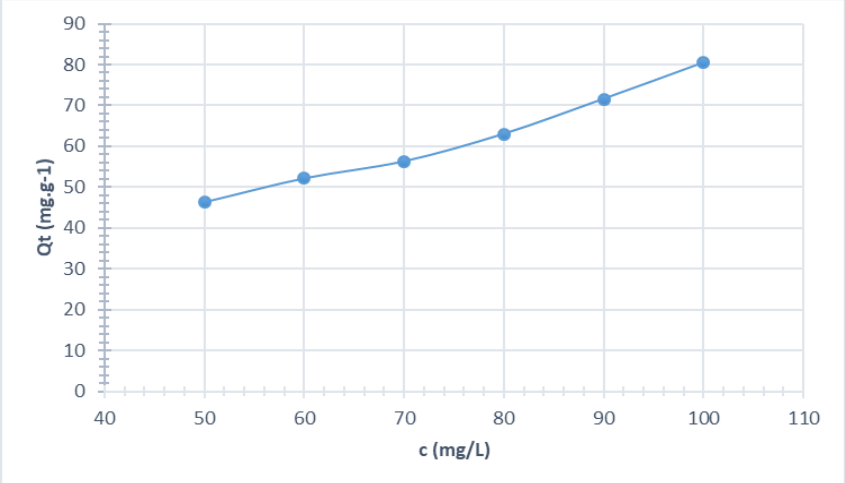


Figure 13. Effect of initial adsorbate concentration on Indigo Carmine (IC) removal.

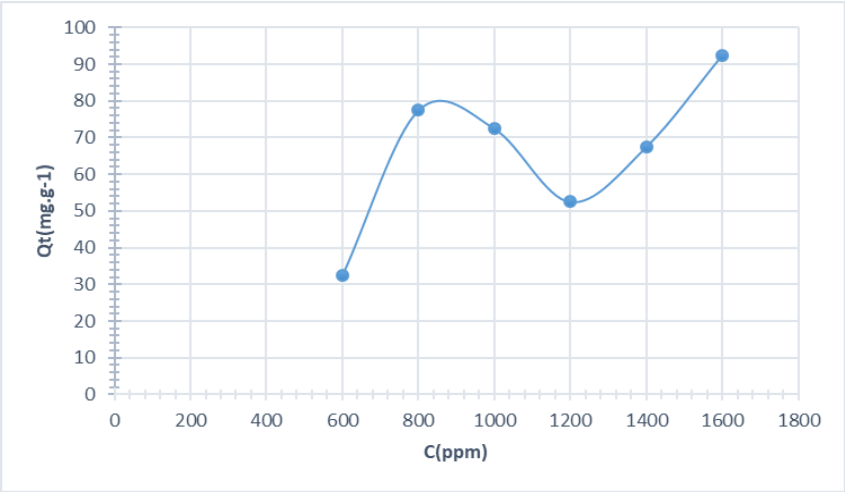


Figure 14. Effect of initial metal concentration on Copper(II) ion removal.

Table 6. Comparison of maximum experimental adsorption capacities (Qe) of IC and Cu(II) ions on various bio-based adsorbents.

Adsorbent	Adsorbate	Qe (mg/g)	Reference
Ricinodendron heudelotii shells AC	IC	133.47	Ankoro *et al.* (2020)
Cetyltrimethylammonium-modified palm oil fiber	IC	128.44	Ngaha *et al.* (2019)
Carbonaceous material	IC	92.83	Gutiérrez-Segura *et al.* (2009)
H_3PO_4-activated cocoa pod (ACP)	**IC**	**80.42**	**Present study**
Pistia stratiotes dry biomass	IC	41.20	Rachel *et al.* (2019)
Brazil nut shells	IC	1.09	De Oliveira Brito *et al.* (2010)
H_3PO_4-activated cocoa pod (ACP)	**Cu(II)**	**167.50**	**Present study**
Peanut hull	Cu(II)	21.25	Zhu *et al.* (2010)
Cashew nut shell	Cu(II)	20.00	SenthilKumar *et al.* (2010)
Cinnamomum camphora leaf powder	Cu(II)	16.76	Chen *et al.* (2010)
Rice shell	Cu(II)	1.85	Aydin *et al.* (2008)

3.4 Post-adsorption FTIR, isotherm, and kinetic modeling

Comparison of FTIR spectra before and after Cu(II) (**Figure 15**) and IC (**Figure 16**) adsorption revealed noticeable peak attenuation and the disappearance of the phosphate/ether band at 1070 cm^{-1}, confirming direct chemical coordination between surface oxygen/phosphorus groups and the adsorbed species. Equilibrium isotherms (**Figures 17–18** and **Table 7**) yielded favorable Freundlich exponents (1/n = 0.313 for IC; 0.681 for Cu(II)), though moderate R^2 values (0.504–0.768) indicate multi-step surface saturation across heterogeneous pores.

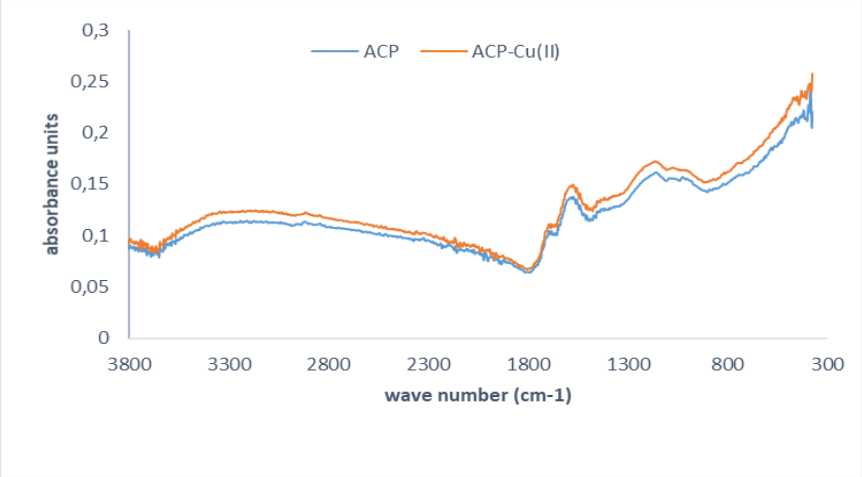


Figure 15. FTIR spectra of ACP before and after Copper(II) ion adsorption.

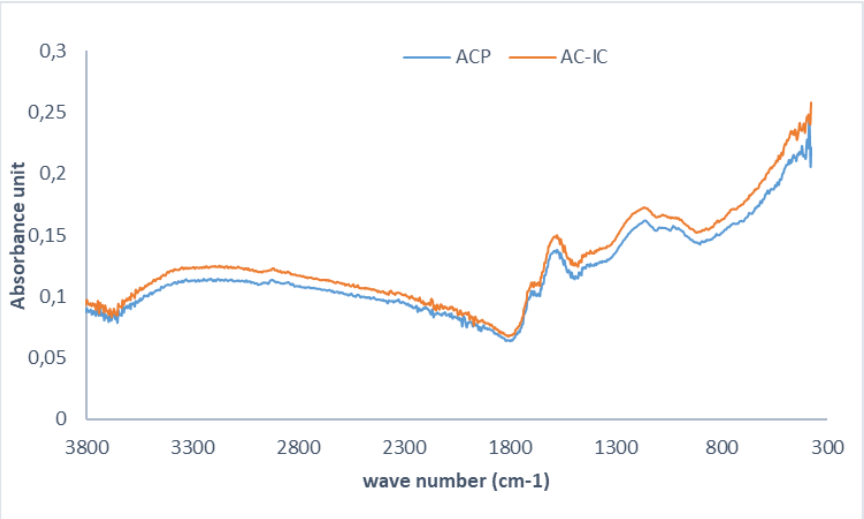


Figure 16. FTIR spectra of ACP before and after Indigo Carmine (IC) adsorption.

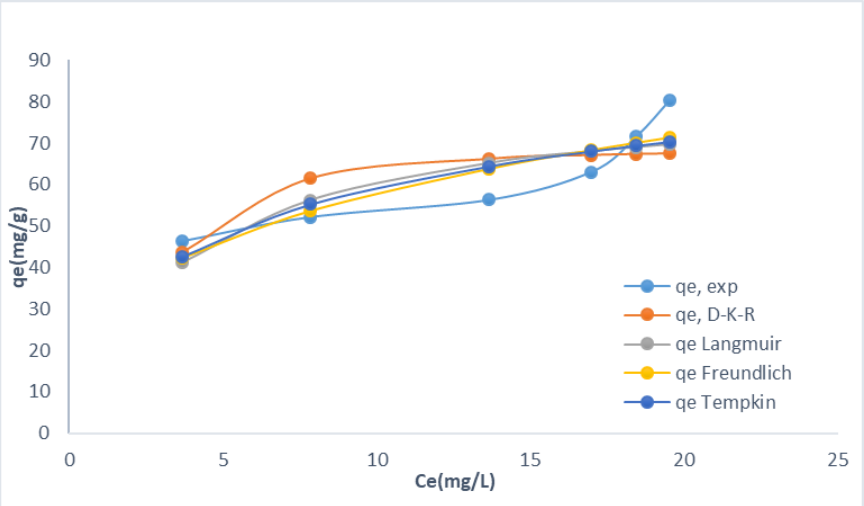


Figure 17. Nonlinear equilibrium isotherm fits for Indigo Carmine (IC) adsorption onto ACP.

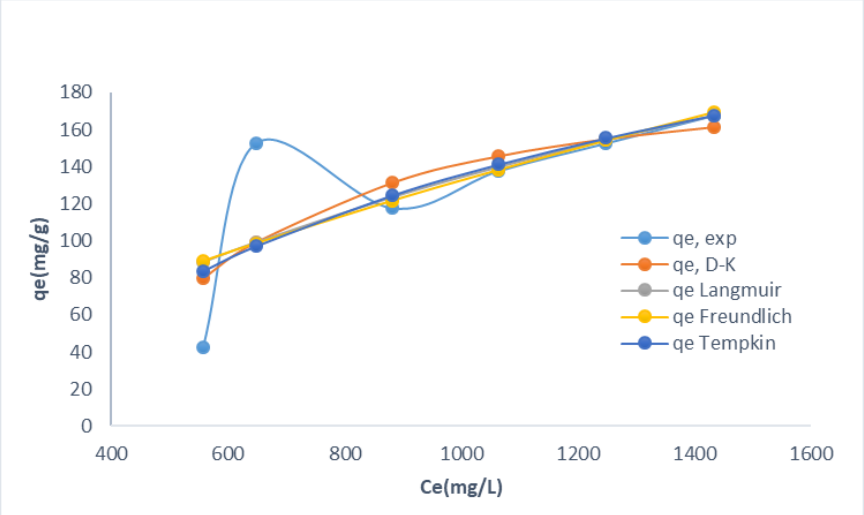


Figure 18. Nonlinear equilibrium isotherm fits for Copper(II) ion adsorption onto ACP.

Nonlinear kinetic fits (**Figures 19–20** and **Table 8**) show that equilibrium was attained within 35 min for Cu(II) and 40 min for IC. The Elovich model yielded the highest determination coefficients (R^2 = 0.979 for IC; R^2 = 0.991 for Cu(II)) and the lowest error functions (RMSE = 2.523 and 4.029; $\chi 2$ = 1.172 and 1.280). The markedly higher initial adsorption rate constants (α = 6152.14 and 4697.89 mg·g-1·min-1) relative to desorption constants (β = 0.176 and 0.062 g/mg) confirm irreversible surface chemisorption on energetically heterogeneous active sites (Ankoro *et al.*, 2020; Zaaboul *et al.*, 2024).

Table 7. Nonlinear equilibrium isotherm parameters for IC and Cu(II) adsorption onto ACP.

Isotherm Model	Parameter	Indigo Carmine (IC)	Copper(II) Ions (Cu2+)
Langmuir	Qm (mg/g)	82.890	390.078
	KL (L/mg)	0.269	0.001
	R^2 / RMSE / $\chi 2$	0.666 / 8.204 / 4.278	0.512 / 35.391 / 4238.457
Freundlich	KF ((mg/g)(L/mg)-1/n)	28.145	1.198
	1/n	0.313	0.681
	R^2 / RMSE / $\chi 2$	0.768 / 6.830 / 2.896	0.504 / 35.694 / 53.988
Temkin	KT (L/mg) / bT (kJ/mol)	3.503 / 3149.205	0.005 / 28.041
	R^2 / RMSE / $\chi 2$	0.718 / 7.541 / 3.497	0.528 / 34.810 / 52.500
Dubinin-Radushkevich	Qm (mg/g) / E (kJ/mol)	68.812 / 5.04×10-4	183.013 / 0.059
	R^2 / RMSE / $\chi 2$	0.512 / 6.038 / 9.910	0.556 / 48.589 / 33.746

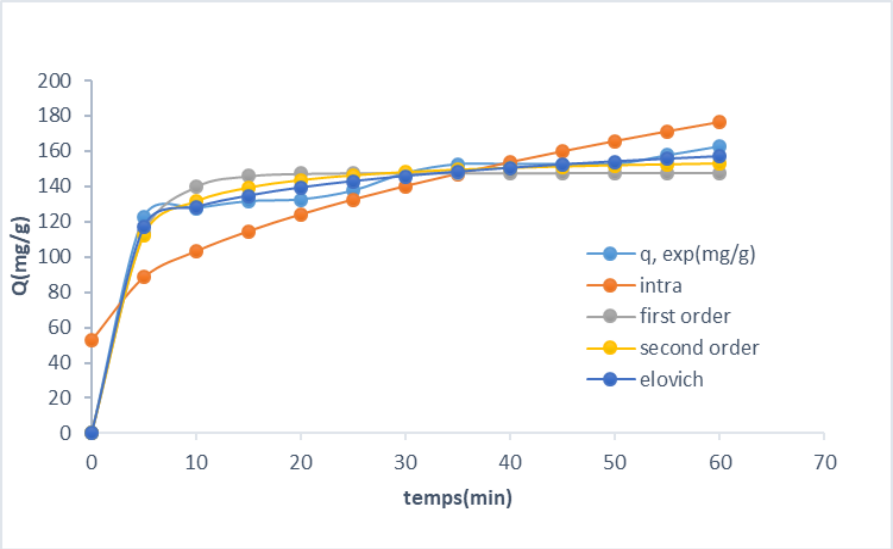


Figure 19. Nonlinear kinetic model fits for Copper(II) ion adsorption onto ACP.

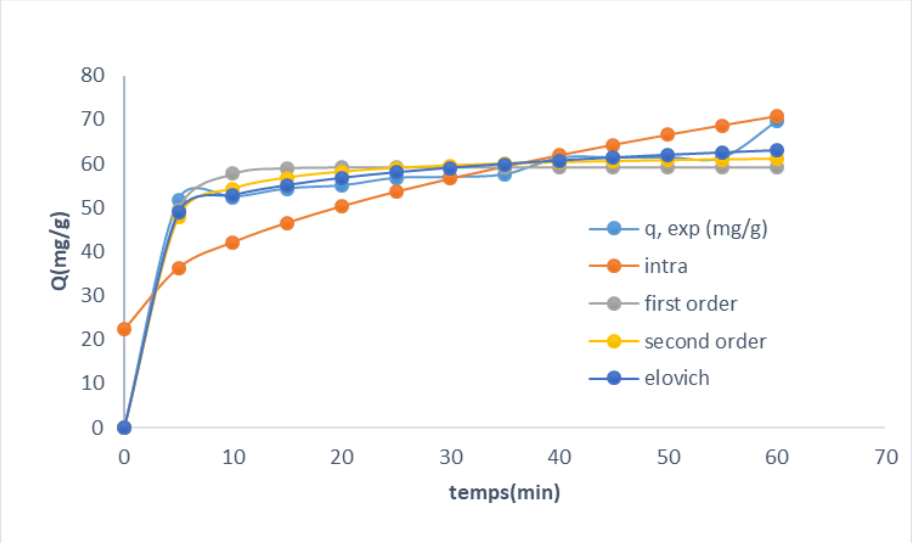


Figure 20. Nonlinear kinetic model fits for Indigo Carmine (IC) adsorption onto ACP.

Table 8. **Nonlinear kinetic parameters for IC and Cu(II) adsorption onto ACP.**

Kinetic Model	Parameter	Indigo Carmine (IC)	Copper (II) Ions (Cu^{2+})
Pseudo-First Order	Qe,pred (mg/g) / k1 (min-1)	59.197 / 0.364	147.710 / 0.293
	R^2 / RMSE / $\chi 2$	0.934 / 4.383 / 3.599	0.942 / 10.312 / 8.160
Pseudo-Second Order	Qe,pred (mg/g) / k2 (g/mg·min)	62.577 / 0.010	156.994 / 0.003
	R^2 / RMSE / $\chi 2$	0.961 / 3.411 / 2.197	0.975 / 6.828 / 3.725
Elovich	**α (mg/g·min) / β (g/mg)**	**6152.137 / 0.176**	**4697.888 / 0.062**
	R^2 / RMSE / $\chi 2$	0.979 / 2.523 / 1.172	0.991 / 4.029 / 1.280
Intra-Particle Diffusion	kid (mg/g·min0.5) / Ci (mg/g)	6.242 / 22.377	15.922 / 52.899
	R^2 / RMSE / $\chi 2$	0.932 / 9.635 / 12.370	0.943 / 22.564 / 26.090

Conclusion

Activated carbon (ACP) was successfully synthesized from Cameroonian cocoa pod husks via H_3PO_4 chemical activation optimized through a Box-Behnken experimental design. Optimal synthesis conditions were established at an impregnation ratio of 1.3, carbonization temperature of 333 °C, and residence time of 1 hour. Physicochemical characterization confirmed a rough, porous morphology (SEM), complete lignocellulosic conversion (TGA-DSC), phosphorus- and oxygen-enriched surface functional groups (FTIR), and an acidic surface character (pHPZC = 3.55). Batch adsorption tests achieved equilibrium within 35–40 min, yielding maximum removal capacities of 80.42 mg/g for Indigo Carmine at pH 2.0 and 167.50 mg/g for Cu(II) ions at pH 4.5. Kinetic modeling demonstrated that the Elovich equation best describes the uptake of both pollutants (R^2 = 0.979–0.991), which together with post-adsorption FTIR spectral shifts confirms chemisorption on an energetically heterogeneous surface as the dominant mechanism.

Acknowledgement: The authors sincerely thank the technical staff and research team of the Applied Physical and Analytical Chemistry Laboratory, University of Yaoundé I (Cameroon), for their laboratory facilities and analytical support.

Disclosure statement: *Conflict of Interest:* The authors declare that there are no conflicts of interest regarding the publication of this manuscript. *Compliance with Ethical Standards:* This article does not contain any studies involving human or animal subjects.

References

Abéga A. V., Ndi J. N., Ngomo H. M. (2015) The performance of activated carbon based cola nuts shells for the removal of Co(II) and Ni(II) ions from aqueous solution, *J. Innov. Sci. Eng.*, 676–683.

Abo El Naga A. O., El Saied M., Shaban S. A., El Kady F. Y. (2019) Fast removal of diclofenac sodium from aqueous solution using sugar cane bagasse-derived activated carbon, *J. Mol. Liq.*, 285, 9–19. https://doi.org/10.1016/j.molliq.2019.04.062

Ahmad M. A., Alrozi R. (2010) Optimization of preparation conditions for mangosteen peel-based activated carbons for the removal of Remazol Brilliant Blue R using response surface methodology, *Chem. Eng. J.*, 165(3), 883–890. https://doi.org/10.1016/j.cej.2010.10.049

Ahmadi S., Ganjidoust H. (2021) Using banana peel waste to synthesize BPAC/ZnO nanocomposite for photocatalytic degradation of Acid Blue 25: influential parameters, mineralization, biodegradability studies, *J. Environ. Chem. Eng.*, 9(5), 106010. https://doi.org/10.1016/j.jece.2021.106010

Akartasse N., Azzaoui K., Mejdoubi E., *et al.* (2022), Environmental-Friendly Adsorbent Composite Based on Hydroxyapatite/Hydroxypropyl Methyl-Cellulose for Removal of Cationic Dyes from an Aqueous Solution, *Polymers*, 14(11), 2147; https://doi.org/10.3390/polym14112147

Ankoro N. O., Kouotou D., Belibi B. P., Ndi J. N., Ketcha J. M. (2016) Removal of indigo carmine dye (IC) by batch adsorption onto dried cola nut shells and its active carbon from aqueous solution medium, *Int. J. Eng. Sci. Res. Technol.*, 5(3), 874–888.

Ankoro N. O., Kouotou D., Lunga P. K., Godwin A. T., Lékéné N. R., Ndi J. N., Ketcha J. M. (2020) Effect of doping activated carbon based Ricinodendron heudelotii shells with AgNPs on the adsorption of indigo carmine and its antibacterial properties, *Arabian J. Chem.*, 13(5), 5241–5253. https://doi.org/10.1016/j.arabjc.2020.03.002

Arivoli S., Nandhakumar V., Saravanan S., Sulochana N. (2009) Adsorption dynamics of copper ion by low cost activated carbon, *Arabian J. Sci. Eng.*, 34(1A), 1–12.

Athéba G. P., Allou N. B., Dongui B. K., Kra D. O., Gbassi K. G., Trokourey A. (2015) Adsorption du butylparabène sur du charbon actif à base des coques de coco provenant de Côte d'Ivoire, *Int. J. Innov. Sci. Res.*, 13(2), 530–541.

Aydin H., Bulut Y., Yerlikaya Ç. (2008) Removal of copper (II) from aqueous solution by adsorption onto low-cost adsorbents, *J. Environ. Manage.*, 87(1), 37–45. https://doi.org/10.1016/j.jenvman.2007.01.005

Berrahou, S., Latifi, S., Saoiabi, S. *et al.* (2026). HAp@Cell bio-films engineered from local resources involving molecular mechanisms of dye adsorption and antibacterial activity. *Sci Rep* 16, 12927, https://doi.org/10.1038/s41598-026-42483-2

Chen H., Zhao J., Dai G., Wu J., Yan H. (2010) Adsorption characteristics of Pb(II) and Cu(II) from aqueous solution onto a natural biosorbent, fallen Cinnamomum camphora leaves, *Desalination*, 262(1–3), 174–182. https://doi.org/10.1016/j.desal.2010.06.006

De Oliveira Brito S. M., Andrade H. M. C., Soares L. F., de Azevedo R. P. (2010) Brazil nut shells as a new biosorbent to remove methylene blue and indigo carmine from aqueous solutions, *J. Hazard. Mater.*, 174(1–3), 84–92. https://doi.org/10.1016/j.jhazmat.2009.09.020

DESA (2020) *Annuaire des Statistiques du Secteur Agricole*, Direction des Enquêtes et des Statistiques Agricoles, MINADER, Yaoundé, Cameroun.

FAOSTAT (2020) *Food and Agriculture Organization Corporate Statistical Database: Crops Production Data*, FAO, Rome.

Gutiérrez-Segura E., Solache-Ríos M., Colín-Cruz A. (2009) Sorption of indigo carmine by a Fe-zeolitic tuff and carbonaceous material from pyrolyzed sewage sludge, *J. Hazard. Mater.*, 170(2–3), 1227–1235. https://doi.org/10.1016/j.jhazmat.2009.05.102

Harrache Z., Abbas M., Aksil T., Trari M. (2019) Thermodynamic and kinetics studies on adsorption of indigo carmine from aqueous solution by activated carbon, *Microchem. J.*, 144, 180–189. https://doi.org/10.1016/j.microc.2018.09.004

Hashem A. H., Saied E., Hasanin M. S. (2020) Green and ecofriendly bio-removal of methylene blue dye from aqueous solution using biologically activated banana peel waste, *Sustain. Chem. Pharm.*, 18, 100333. https://doi.org/10.1016/j.scp.2020.100333

Jiang Y., Qin Z., Liang F., Li F., Sun Y., Wang X., Ma P., Song D. (2021) Vortex-assisted solid-phase extraction based on metal-organic framework/chitosan functionalized hydrophilic sponge column for determination of triazine herbicides in environmental water by liquid chromatography-tandem mass spectrometry, *J. Chromatogr. A*, 1638, 461887. https://doi.org/10.1016/j.chroma.2021.461887

Kouotou D., Ngomo H. M., Baçaoui A., Yaacoubi A., Ketcha J. M. (2013) Optimization of activated carbons prepared by H3PO4 and steam activation of oil palm shell, *J. Chem.*, 2013, 654343. https://doi.org/10.1155/2013/654343

Lékéné N. R. B., Ndi J. N., Rauf A., Kouotou D., Belibi B. P. D., Bhanger M. I., Ketcha J. M. (2018) Optimization conditions of activated carbon based Egusi (Cucumeropsis mannii Naudin) seed shells for nitrite ions removal from wastewater, *Am. J. Anal. Chem.*, 9(10), 439–463. https://doi.org/10.4236/ajac.2018.910034

León O., Muñoz-Bonilla A., Soto D., Pérez D., Rangel M., Colina M., Fernández-García M. (2018) Removal of anionic and cationic dyes with bioadsorbent oxidized chitosans, *Carbohydr. Polym.*, 194, 375–383. https://doi.org/10.1016/j.carbpol.2018.04.072

Li H., An N., Liu G., Li J., Liu N., Jia M., Zhang W., Yuan X. (2016) Adsorption behaviors of methyl orange dye on nitrogen-doped mesoporous carbon materials, *J. Colloid Interface Sci.*, 466, 343–351. https://doi.org/10.1016/j.jcis.2015.12.048

Maazou B. S., Hima H. I., Alma M. M. M., Natatou I. (2017) Élimination du chrome par du charbon actif élaboré et caractérisé à partir de la coque du noyau de Balanites aegyptiaca, *Int. J. Biol. Chem. Sci.*, 11(6), 3050–3065. https://doi.org/10.4314/ijbcs.v11i6.39

Mashile G. P., Mpupa A., Nomngongo P. N. (2021) Magnetic mesoporous carbon/β-cyclodextrin–chitosan nanocomposite for extraction and preconcentration of multi-class emerging contaminant residues in environmental samples, *Nanomaterials*, 11(2), 540. https://doi.org/10.3390/nano11020540

Mohammed Jaafar A. A., Al-Sharify Z. T. (2019) Utilization of low cost adsorbents for the adsorption process of lead ions, *Int. J. Mod. Res. Eng. Technol.*, 4(11), 29–48.

Ndifor-Angwafor N. G., Tiotsop I. H., Tchuifon R. D., Ngakou C., Bopda A., Kamdem A. T., Anagho S. G. (2017) Biosorption of amaranth red in aqueous solution onto treated and untreated lignocellulosic materials (pineapple peelings and coconut shells), *J. Mater. Environ. Sci.*, 8(12), 4199–4212.

Ngaha M. C. D., Njanja E., Doungmo G., Kamdem T., Tonleu I. K. (2019) Indigo carmine and 2,6-dichlorophenolindophenol removal using cetyltrimethylammonium bromide-modified palm oil fiber: Adsorption isotherm and mass transfer kinetics, *Int. J. Biomater.*, 2019, 6862825. https://doi.org/10.1155/2019/6862825

Ousmaila S. M., Adamou Z., Ibrahim D., Ibrahim N. (2016) Préparation et caractérisation de charbons actifs à base de coques de noyaux de Balanites aegyptiaca et de Zizyphus mauritiana, *J. Soc. Ouest-Afr. Chim.*, 41, 59–67.

Puziy A. M., Poddubnaya O. I., Martínez-Alonso A., Suárez-García F., Tascón J. M. D. (2005) Synthetic carbons prepared by phosphoric acid activation. Part 1. Surface and chemical characterization, *Carbon*, 43(7), 1407–1412. https://doi.org/10.1016/j.carbon.2004.12.037

Rashid R., Shafiq I., Akhter P., Iqbal M. J., Hussain M. (2021) A state-of-the-art review on wastewater treatment techniques: the effectiveness of adsorption method, *Environ. Sci. Pollut. Res.*, 28(8), 9050–9066. https://doi.org/10.1007/s11356-021-12395-x

SenthilKumar P., Ramalingam S., Senthamarai C., Niranjanaa M., Vijayalakshmi P., Sivanesan S. (2010) Adsorption of dye from aqueous solution by cashew nut shell: Studies on equilibrium isotherm, kinetics and thermodynamics of interactions, *Desalination*, 261(1–2), 52–60. https://doi.org/10.1016/j.desal.2010.05.032

Wong S., Ngadi N., Inuwa I. M., Hassan O. (2018) Recent advances in applications of activated carbon from biowaste for wastewater treatment: A short review, *J. Cleaner Prod.*, 175, 361–375. https://doi.org/10.1016/j.jclepro.2017.12.059

Zaaboul F., Canle M., Haoufazane C., Santaballa J.A., Hammouti B., Azzaoui K., Jodeh S., Hadjadj A., El Hourch A. (2024), Sunlight-driven photodegradation of RB49 dye using TiO2-P25 and TiO2-UV100: Performance comparison, *Coatings*, 14(10), 1270. https://doi.org/10.3390/coatings14101270

Zhu G. Z., Deng X. L., Hou M., Sun K., Zhang Y. P., Li P., Liang F. M. (2016) Comparative study on characterization and adsorption properties of activated carbons by phosphoric acid activation from corncob and its acid and alkaline hydrolysis residues, *Fuel Process. Technol.*, 144, 255–261. https://doi.org/10.1016/j.fuproc.2016.01.007

Zulfiqar M., Samsudin M. F. R., Sufian S. (2019) Modelling and optimization of photocatalytic degradation of phenol via TiO2 nanoparticles: An insight into response surface methodology and artificial neural network, *J. Photochem. Photobiol. A*, 384, 112039. https://doi.org/10.1016/j.jphotochem.2019.112039